RESEARCH ARTICLE

Key Points:
- The AirSWOT experimental airborne Ka-band radar interferometer maps water surface elevations and slope, enabling study of lake, river, and wetland flow gradients
- AirSWOT is a useful validation instrument for the SWOT satellite mission (launch 2021), especially in rivers
- AirSWOT hardware remains experimental, but recommended modifications to processing, calibration, and experiment design may improve precisions

Supporting Information:
- Supporting Information S1
- Data Set S1

Correspondence to:
L. H. Pitcher,
lincolnpitcher@ucla.edu

AirSWOT InSAR Mapping of Surface Water Elevations and Hydraulic Gradients Across the Yukon Flats Basin, Alaska

Lincoln H. Pitcher[1], Tamlin M. Pavelsky[2], Laurence C. Smith[1], Delwyn K. Moller[3], Elizabeth H. Altenau[2], George H. Allen[2], Christine Lion[2], David Butman[4], Sarah W. Cooley[5], Jessica V. Fayne[1], and Mark Bertram[6]

[1]Department of Geography, University of California, Los Angeles, CA, USA, [2]Department of Geological Sciences, University of North Carolina at Chapel Hill, Chapel Hill, NC, USA, [3]Remote Sensing Solutions, Monrovia, CA, USA, [4]Department of Civil and Environmental Engineering, University of Washington, Seattle, WA, USA, [5]Institute at Brown for Environment and Society, Brown University, Providence, RI, USA, [6]Yukon Flats National Wildlife Refuge, US Fish and Wildlife Service, Fairbanks, AK, USA

Abstract AirSWOT, an experimental airborne Ka-band interferometric synthetic aperture radar, was developed for hydrologic research and validation of the forthcoming Surface Water and Ocean Topography (SWOT) satellite mission (to be launched in 2021). AirSWOT and SWOT aim to improve understanding of surface water processes by mapping water surface elevation (WSE) and water surface slope (WSS) in rivers, lakes, and wetlands. However, the utility of AirSWOT for these purposes remains largely unexamined. We present the first investigation of AirSWOT WSE and WSS surveys over complex, low-relief, wetland-river hydrologic environments, including (1) a field-validated assessment of AirSWOT WSE and WSS precisions for lakes and rivers in the Yukon Flats Basin, an Arctic-Boreal wetland complex in eastern interior Alaska; (2) improved scientific understanding of surface water flow gradients and the influence of subsurface permafrost; and (3) recommendations for improving AirSWOT precisions in future scientific and SWOT validation campaigns. AirSWOT quantifies WSE with an RMSE of 8 and 15 cm in 1 and 0.0625 km^2 river reaches, respectively, and 21 cm in lakes. This indicates good utility for studying hydrologic flux, WSS, geomorphic processes, and coupled surface/subsurface hydrology in permafrost environments. This also suggests that AirSWOT supplies sufficient precision for validating SWOT WSE and WSS over rivers, but not lakes. However, improvements in sensor calibration and flight experiment design may improve precisions in future deployments as may modifications to data processing. We conclude that AirSWOT is a useful tool for bridging the gap between field observations and forthcoming global SWOT satellite products.

1. Introduction

Understanding surface water hydrological processes is critical for natural and engineered ecosystems (Cisneros et al., 2014; Gleason et al., 2017), yet empirical measurements of large-scale surface water storage, transport, and dynamics remain limited (Pekel et al., 2016). To that end, AirSWOT, an experimental airborne Ka-band radar interferometer uniquely engineered to map water surface elevation (hereafter called WSE), has been developed both to enhance scientific understanding of lake, wetland, and river floodplain hydrology and as a potential validation tool for the forthcoming Surface Water Ocean Topography (SWOT) satellite mission. SWOT is a joint international effort of the National Aeronautics and Space Administration (NASA), Centre National d'Etudes Spatiales, Canadian Space Agency, and United Kingdom Space Agency with anticipated launch in 2021. Its nominal goal is to map global freshwater storage and transport in rivers and lakes every ~21 days (Biancamaria et al., 2016). For their core measurements, both AirSWOT and SWOT use 35-GHz Ka-band radar interferometers to produce swath-based mappings of WSE, which is used to derive water surface slope (hereafter called WSS), two hydrologic variables essential for quantifying storage and flux of terrestrial inland surface water.

This study deployed AirSWOT and a field team to eastern interior Alaska in June 2015 for testing over the Yukon Flats Basin (YFB), a protected wetland area within the Yukon Flats National Wildlife Refuge, which straddles the Arctic circle (Figure 1a). The YFB has complex, low-relief topography and is underlain by
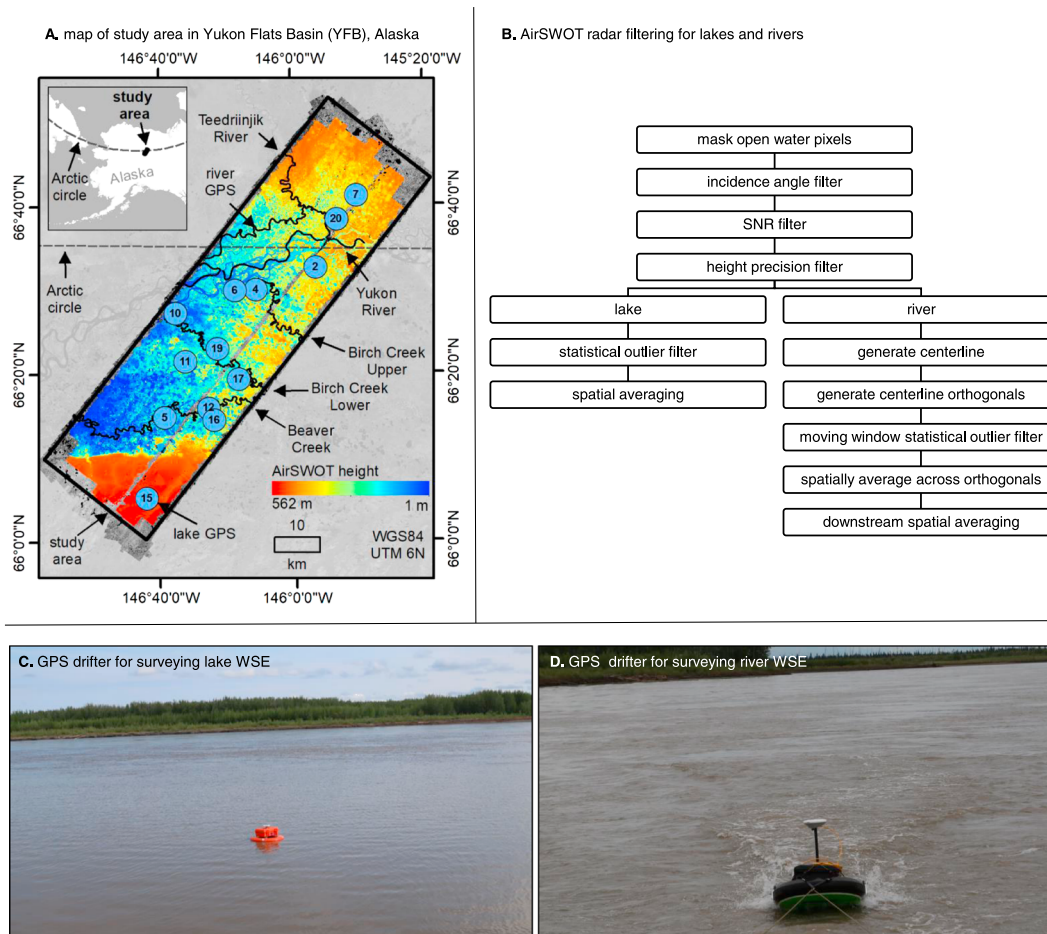
Figure 1. (a) AirSWOT mapping extent (black box) in the YFB, eastern interior Alaska, USA. Underlying image is the AirSWOT DEM overlaid on the near-infrared band from a color-infrared orthomosiac generated using images collected coincident with AirSWOT radar data (Table 1). Background image is a Landsat-8 OLI mosaic. The locations of 13 lakes surveyed in situ are shown (blue circles with numeric identifiers). The Yukon River water surface elevation (WSE) global positioning system (GPS) survey is plotted along with the other river profiles assessed, namely, Yukon River main channel, Birch Creek-Upper, Birch Creek-Lower, Beaver Creek, and the Teedriinjik River. The dashed gray line denotes the Arctic circle boundary, which is ~66.57 °N. The inset shows the location of the study area in eastern interior Alaska. (b) AirSWOT data quality filtering and spatial averaging flowchart for lakes (left) and rivers (right). (c) The custom GPS system used to survey 13 lakes across the YFB between 27 May 2015 and 12 June 2015. (d) The custom GPS system mounted on a SonTek/YSI Hydroboard II that we escort down an ~82-km reach of the Yukon River and a lateral distributary channel towed behind a motorized river boat.

discontinuous permafrost (Gulbrandsen et al., 2016; Minsley et al., 2012; Pastick et al., 2013). It is characterized by hydrologically connected and disconnected lakes (Cooley et al., 2017), remnant oxbows (Brabets et al., 2000), and intermittently inundated lakes and wetlands (Jepsen et al., 2016). Our study area is crossed by a large anabranching reach of the Yukon River and a network of tributary channels, all referred to as *rivers* (Figure 1a). The global significance of Arctic-Boreal wetlands like the YFB is underscored by the key roles that lakes and rivers play in greenhouse gas exchanges with the atmosphere (Raymond et al., 2013) and the related impact of permafrost thaw on changing surface extent and groundwater fluxes (Smith et al., 2007; Walvoord et al., 2012). For these reasons, we directed AirSWOT deployments to the YFB as both a test of instrument performance and to enhance scientific understanding of surface water interactions in a complex wetland environment underlain by discontinuous near-surface permafrost.

AirSWOT deploys a Ka-band SWOT Phenomenology Airborne Radar (KaSPAR) sensor, a digital camera system that collects high-resolution color infrared (CIR) imagery, and a precision internal motion unit (https://swot.jpl.nasa.gov/airswot.htm). KaSPAR has a 5-km swath width with incidence angles ranging from 2° to 25° (Neeck et al., 2012). The KaSPAR data are postprocessed using InSAR software at the NASA Jet Propulsion Laboratory to produce a uniformly gridded WSE data product, here processed to 3.6-m pixels. AirSWOT

thus has a broader incidence angle range and considerably higher resolution than SWOT, which will have a native range resolution of 10–60 m, an azimuth resolution of 6–7 m, and an incidence angle range of 0.6–3.9° (Biancamaria et al., 2016; Fjørtoft et al., 2014). AirSWOT is thus not a direct analog for SWOT but yields similar types of measurements offering a unique opportunity to study Ka-band returns and assess the scientific value of WSE and WSS measurements in poorly understood wetland environments such as the YFB.

Like all scientific satellite missions, SWOT is designed to meet predefined accuracy standards. The accuracy standards of SWOT relevant to this work include quantification of WSE to ±10-cm vertical accuracy per 1 km^2 open water area, WSE to ±25-cm vertical accuracy per 0.0625 km^2 open water area, and WSS to an accuracy of ±1.7 cm/km when averaged over 10-km reaches that are at least 100 m wide (Rodriguez, 2016). Therefore, an important objective of this research is to examine whether AirSWOT measurements of WSE and WSS meet or exceed SWOT standards, which will help determine if AirSWOT is a suitable instrument platform to validate SWOT.

Between 27 May and 15 June 2015, we collected in situ pressure transducer (PT) and global positioning system (GPS) field surveys of WSE in YFB lakes and rivers and then deployed AirSWOT over these same sites on 15 June 2015. These field and remotely sensed data sets are used to answer four questions: (1) Can AirSWOT measurements resolve WSE and WSS in lakes and rivers with sufficient precision to validate SWOT? (2) What factors contribute to variations in AirSWOT precision? (3) Can AirSWOT images be used to improve scientific understanding of surface water flow through complex Arctic-Boreal wetland systems? (4) How might AirSWOT precisions be improved in future campaigns?

To address these questions, we first compare AirSWOT WSE with PT-corrected GPS surveys in 13 lakes (referred to as PT WSE) as well as a GPS survey along an ~82-km reach of the Yukon River and a lateral distributary channel (referred to as GPS WSE). Second, we evaluate how spatial averaging of AirSWOT data impacts precision. Third, we assess the influence of permafrost on WSE variability across the YFB and examine longitudinal river profiles for fluvial geomorphological investigation. We also evaluate the utility of InSAR imaging as a demonstration of AirSWOT's potential contributions to basic hydrologic research. Finally, we conclude with a discussion of the strengths and limitations of using AirSWOT to validate SWOT, how AirSWOT data precisions may be improved in the future, and the scientific potential for AirSWOT independent of the SWOT mission.

2. Data and Methods

This research uses remotely sensed imagery collected with AirSWOT and other remote sensing platforms, in situ field measurements, and ancillary model data. These data sets are outlined in Table 1, and our processing procedures are detailed in the sections to follow.

2.1. AirSWOT Data Collection and Processing

On 15 June 2015, AirSWOT data were collected over a ~3,300-km^2 area of the YFB (Figure 1a). The surveyed area was ~30 km east-to-west and ~110 km north-to-south and was mapped using 10 overpasses or paths (Figure S2b in the supporting information). The CIR, internal motion unit, and KaSPAR instruments were mounted on a King Air B200 aircraft operated by NASA Armstrong (Dryden) Flight Research Center. The radar data were processed at Jet Propulsion Laboratory using custom, AirSWOT-specific InSAR software to yield standard data products of height in meters above the WGS84 ellipsoid, radar backscatter (dB), incidence angle (°), and random height error (or precision, derived from the interferometric correlation; Rosen et al., 2000; m). Likewise, we derived signal to noise (SNR) as the difference between backscatter and noise equivalent backscatter. AirSWOT data layers are summarized in Table 1 and available via the Oak Ridge National Laboratory Distributed Active Archive Center for Biogeochemical Dynamics (Pitcher et al. 2018).

Comparisons of AirSWOT to in situ WSE and WSS required data quality filtering of AirSWOT incidence angle, error, SNR, and height outliers (Figure 1b). First, we exclude all pixels with incidence angles <5° and >20°. Near-nadir (<5°) pixels were excluded because data processing limitations result in inconsistent height retrievals at these incidence angles. Data for angles >20° were excluded due to sensitivity of the antenna pattern roll off when coupled with aircraft roll. Next, we remove pixels with low SNR (<5 dB) and random height error >1 m.

Table 1
Summary of Data Used, Including Data Abbreviation (When Given), Data Resolution, Use and Data Source

Category	Name	Code	Info	Use	Source
AirSWOT and satellite optical imagery	Cirrus Digital Systems color-infrared (CIR) multiband imagery	CIR	Pixel size: 3.6 m (resampled) Bands (or channels): 3 Band 1: nir Band 2: red Band 3: green Band 4: data mask units: DN	Generate masks for open water AirSWOT extraction	Collected coincident with AirSWOT radar data; data provided by Cirrus Digital Systems
	Landsat OLI	OLI	Projection: WGS84 UTM6N Pixel size: 30 m Band 5: nir (only band used) Units: DN	Data visualization and mapping	Images collected 15–17 June 2015, data acquired from USGS GloVis
AirSWOT interferometric Ka-band radar data (KaSPAR)	Height	WSE	projection: WGS84 UTM6N Pixel size: 3.6 m Units: m relative to WGS84 Projection: WGS84 UTM6N	Estimate WSE	Processed AirSWOT radar data provided by NASA/JPL
	Precision (or error)	ε	Pixel size: 3.6 m Units: m Projection: WGS84 UTM6N	AirSWOT data filtering	
	Incidence Angle	$\angle$	Pixel size: 3.6 m. Units: degrees (°) Projection: WGS84 UTM6N * Converted original data to degree from radians		
	Radar backscatter		Pixel size: 3.6 m. Units: dB Projection: WGS84 UTM6N *Converted original data to dB with equation $20*\log10(\text{magnitude})$		
	Noise equivalent radar backscatter		Pixel size: na Units: dB Projection: na Data provided as netcdf		
	Signal-to-noise ratio	SNR	with $\angle$ Pixel size: 3.6 m. Units: dB Projection: WGS84 UTM6N *Calculated as the difference between backscatter and noise equivalent backscatter		
Digital elevation models (DEMs)	ArcticDEM	ArcticDEM	Pixel Size: 5 m Units: m relative to WGS84 Projection: WGS84 UTM6N	AirSWOT radar phase unwrapping, layover simulaiton	ArcticDEM version 1.0 with data gap interpolation. Data available from the Polar Geospatial Center
	MERIT DEM	MERIT	Pixel size: 60 m (resampled) Projection: WGS84 UTM6N (reprojected)	hydraulic gradient and permafrost analysis	Yamazaki et al., (2017)
Permafrost	Probability of permafrost presence	Permafrost probability	Pixel size: 30 m	hydraulic gradient and permafrost analysis	Pastick et al., (2013)

Table 1 *(continued)*

Category	Name	Code	Info	Use	Source
Field Data	Yukon Flats water body GPS Surveys Yukon River GPS Surveys	GPS	Projection: Albers Conic Equal Area Datum: WGS84 GPS: Trimble R5700 or R7 Refer to sections 3.3 and 3.4 for data processing and precision details	comparison with AirSWOT WSE	see depth corrected WSE in Table 2 Data Set S1
	Yukon Flats water body depths	water body depth	Solinst levellogger and barologgers. See: https://solinst.com//	GPS WSE corrections	depth offsets given in Table 2
Reference .shp files	Watershed Boundary Data set	WBD	Scale: 1:24,000	separates study area into watersheds	downloaded from USDA Geospatial Data Gateway, also available via USGS

Note. DN = digital number; GPS = global positioning system; JPL = Jet Propulsion Laboratory; NASA = National Aeronautics and Space Administration; SWOT = Surface Water and Ocean Topography; WSE = water surface elevation.

Our data filtering does not explicitly remove pixels contaminated by topographic layover, which is an image distortion that is produced when incidence angles are smaller than a surface slope oriented toward the sensor (Jenson, 2000). However, due to minimal topographic relief across most of the YFB, we expect any layover to be driven primarily by vegetation, which is not reliably measured across our study area. Despite the small anticipated impacts, we simulate layover for one AirSWOT path (Figure S3a) using the approach developed by Sheng et al. (2016) and ArcticDEM as the input surface model. We find that ~33% of layover-contaminated water pixels have incidence angles <5°, which are eliminated by data quality filtering. Moreover, data quality filtering removes >12 times the number of pixels than those with layover (Figure S3b). We also recognize that ArcticDEM does not reliably measure surface heights, particularly in forested areas (Glennie, 2018). Thus, we do not attempt additional corrections for layover. We consider AirSWOT WSE and WSS validation with other remotely sensed data sets (e.g., lidar) inappropriate because remotely sensed data that spatially and temporally overlap 15 June 2015 AirSWOT and accurately measure WSE and WSS are not available.

Our AirSWOT analysis is subdivided into rivers, streams, and channels (collectively referred to as *rivers*) and lakes, wetlands, remnant oxbows, and thermokarst ponds (collectively referred to as *lakes*). To calculate WSE in lakes, we first use an open water mask created from simultaneously collected AirSWOT CIR camera imagery (section 2.2) to select only water pixels from the radar data. Next, we apply a statistical outlier filter that removes AirSWOT WSE pixels >3 median absolute deviations from the median. Finally, the median value of remaining pixels in each lake is calculated. Individual lake masks vary in size from 55.9 m^2 (~4 AirSWOT pixels) to 3.26 km^2 (~251,543 AirSWOT pixels). Refer to Figure S4 for histograms of filtered AirSWOT lake WSEs compared with in situ PT corrected GPS surveys.

We also use the AirSWOT CIR open water mask over rivers to extract only water pixels from the KaSPAR data. Next, we generate cross-section segments orthogonal to the river centerline and average AirSWOT WSE along each orthogonal cross section. The centerline is created using ChanGeom v0.3 (Fisher et al., 2012, 2013). The output from ChanGeom is a raster file with pixel values corresponding to downstream distances starting from the upstream end of the water mask. We use a Polynomial Approximation with Exponential Kernel algorithm (http://pro.arcgis.com/en/pro-app/tool-reference/cartography/smooth-line.htm) to remove right angles in the raster-based centerline. Next, similar to Pavelsky and Smith (2008) and Fisher et al. (2013), we generate orthogonal polylines spanning the width of a river mask at 3.6-m downstream spacing along the river centerline by calculating the negative reciprocal of the slope between downstream centerline points and extending a polyline from a centerline pixel across the river. Lastly, we intersect the derived orthogonal cross sections with AirSWOT data for spatial averaging along the length of the cross section.

For comparison with SWOT accuracy standards, ~0.0625- and ~1-km^2 reaches were established by summing pixel areas in a downstream direction until the area threshold is exceeded. The average and standard deviation of orthogonal means contained within a reach were calculated, and the process was repeated for each centerline orthogonal. The reach start and end downstream distances were used to subset GPS survey points, calculate the average GPS WSE value for each reach, and then compare with spatially averaged AirSWOT WSE. Similarly, slopes were calculated by first subsetting AirSWOT and GPS data according to start and end downstream distances for 10-km reaches established at each centerline orthogonal. Then, a linear model was fit between distance and AirSWOT/GPS WSE.

2.2. AirSWOT Open Water Mask

The AirSWOT instrument suite includes a Cirrus Digital Systems camera (http://cirrus-designs.com/), which collects 16-MP digital images using a Zeiss 60-mm focal length lens with a 34° × 34° field of view. Each CIR digital image contained a near-infrared (nir), red (r), and green (g) band. A radially and relief-corrected ortho-mosaic was generated from 780 individual CIR images using a photogrammetrically generated digital surface model in Agisoft Photoscan Pro. The YFB has minimal topographic relief, and the flight altitude was >8,770 m (Figure S2); therefore, topographic distortion was minimal. The orthomosaic was exported as 16-bit GeoTiffs split into 33 quads, each containing 10,000 × 10,000 pixels with values given as raw digital numbers. To enable comparison with AirSWOT WSE data, the 33 CIR quads were combined into one orthomosaic, assigned a WGS-1984 UTM-6N projection, and resampled to a 3.6-m pixel size.

To limit extraction of AirSWOT WSE to open water pixels only, the CIR data were classified as water or non-water. To achieve this, a normalized difference water index (NDWI) was calculated as

$$NDWI = \frac{g - nir}{g + nir},$$

where g is the green band and nir is the near-infrared band in the CIR data (Mcfeeters, 1996). We then used an automated thresholding technique to classify water. As a first guess, we classified water for 1-km^2 cells in the NDWI using Otsu's threshold selection method (Otsu 1979), then visually inspected this preliminary water mask to remove clouds/shadows falsely identified as water and to separate rivers from lakes. To enhance classification accuracy, a localized NDWI threshold was then calculated for each lake and every 5-km down-stream channel reach. Similar to Li and Sheng (2012), localized search areas were defined with approximately twice the area of each lake and river reach in the preliminary water mask. Next, a threshold value was defined for each local search area (Otsu 1979), and the NDWI was classified as water and nonwater pixels, which were visually inspected for errors. In total, we identified 2,786 lakes across the study area, of which we manually edited 201 to improve classification accuracy.

To further assess water mask accuracy, we digitized boundaries of 50 lakes without manual edits and com-pared open water areas with those automatically extracted. We find strong statistical agreement between autoextracted and manually digitized lake areas ($r^2 > 0.9$, RMSE = 0.01 km^2; Figure S5). We manually modified all river masks to establish single-channel sections for generation of orthogonal cross sections to guide AirSWOT WSE extraction.

2.3. In Situ Lake and River GPS Surveys

Lake water levels were monitored in situ using Solinst Levelogger PTs corrected with average Solinst Barologger barometric pressure readings logged along the shorelines of lake #19 (Canvasback Lake, Figure 1) and 9-Mile Lake (between lakes #5 and #15; Figure 1a). Solinst Levelogger uncertainty is 0.05% to 0.10% full-scale units (model dependent) and barologger uncertainty is 0.51 cm. We calculated WSE uncer-tainty due to logger error as the sum of 0.10% full scale meter applied to the maximum recorded depth, which yielded an uncertainty of 0.7 cm. Levelogger and barologgers were both set to record at 5-min inter-vals. We first removed outlier recordings from the original data series using a moving mean smoothing func-tion and then calculated a daily average water level. The PTs in lakes #4 and #15 appear to move between installation, GPS survey date, and AirSWOT data collection. To correct for this, we calculate a constant depth offset at shifts in the time series and apply this offset to subsequent sections of the recorded water levels (see Figure S6).

Lake water levels were transformed to WSE in meter above the WGS-1984 ellipsoid by adjusting GPS lake WSE surveys performed between 27 May 2015 and 12 June 2015 with depth changes between in situ survey date and the AirSWOT collection. GPS surveys were completed using a custom-designed floating platform con-structed by mounting a ruggedized watertight case on a high-density foam flotation ring and integrating a Trimble R5700 or R7 GPS receiver, a Trimble Zephyr Antenna, and a 12-volt power supply (Figure 1c). We refer to PT-corrected GPS surveys in lakes as PT WSE.

We first processed the lake GPS surveys using the Canadian Spatial Reference System Precise Point Positioning (PPP) web application (https://webapp.geod.nrcan.gc.ca/geod/tools-outils/ppp.php). We used

Table 2
Summary of Field Surveyed Lake Location, Lake Mask Area, AirSWOT WSE, and PT WSE

Lake #	Latitude	Longitude	Lake mask area, km^2	AirSWOT WSE, m	# pixels	PT WSE, m	Depth offset, cm	GPS survey date	PT WSE – AirSWOT WSE, m
2	66.5448	−145.8871	1.80	130.9 ± 0.2	99,876	131.1 ± 0.0	−0.78	06/11/15	0.22
4	66.5012	−146.1861	0.02	121.5 ± 0.2	1,801	121.8 ± 0.1	−0.27	06/12/15	0.34
5	66.2483	−146.6431	0.04	122.6 ± 0.2	2,159	123.1 ± 0.1	−3.92	06/02/15	0.48
6	66.5004	−146.2901	0.10	125.0 ± 0.2	7,048	125.3 ± 0.1	−1.93	06/10/15	0.32
7	66.6868	−145.6761	1.02	132.8 ± 0.2	63,271	133.4 ± 0.1	−1.45	06/11/15	0.51
10	66.4553	−146.5879	0.15	121.5 ± 0.6	3,869	121.5 ± 0.1	−9.20	06/09/15	0.02
11	66.3592	−146.5396	0.01	126.3 ± 0.9	94	126.3 ± 0.0	−3.65	06/09/15	0.05
12	66.2660	−146.4248	0.03	127.1 ± 0.3	1,221	127.4 ± 0.1	−1.48	06/10/15	0.34
15	66.0880	−146.7328	0.86	209.6 ± 0.2	82,944	209.5 ± 0.3	−0.24	06/12/15	−0.14
16	66.2431	−146.3996	3.26	127.7 ± 0.2	128,472	127.7 ± 0.1	−4.97	06/27/15	−0.02
17	66.3234	−146.2756	1.36	129.0 ± 0.3	133,380	129.0 ± 0.1	−1.77	06/09/15	−0.05
19	66.3843	−146.3812	1.98	126.8 ± 0.3	149,267	127.4 ± 0.1	−0.65	06/11/15	0.59
20	66.6398	−145.7777	0.84	129.7 ± 0.2	58,157	130.0 ± 0.1	−20.56	06/11/15	0.27

Note. GPS = global positioning system; PT = pressure transducer; SWOT = Surface Water and Ocean Topography; WSE = water surface elevation. AirSWOT uncertainty is reported as the standard deviation in WSE pixels after data quality filtering. Similarly, number of pixels is the count of remaining pixels in each lake after filtering. Depth offset is the PT measured change in lake level between GPS and AirSWOT surveys.

the Canadian Spatial Reference System PPP solutions to clip the original data series to times when the GPS units were in the water. Next, surveys were subset using the UNAVCO TEQC tool (Estey & Meertens, 1999). The extracted data were then reprocessed with Geodésie par Intégrations Numériques Simultanées (GINS) software using the kinematic integer PPP method (Marty et al., 2011). Kinematic processing mode was selected because GPS lake drifters float on the lake surface and are locally influenced by wind and wave conditions, resulting in nonstationary surveys. A constant offset of 25.65 ± 1.95 cm was applied to each GPS survey to account for the distance from the GPS antenna to the water surface. Adapted from Hopkinson et al. (2011), PT WSE error is calculated as

$$\epsilon = \sqrt{\left(\epsilon_{lv} + \epsilon_{bl}\right)^2 + \left(\epsilon_{gps} + \epsilon_{ant}\right)^2},$$

where ϵ_{lv} is error from the levelogger, ϵ_{bl} is error from the barologger, ϵ_{gps} is maximum GPS uncertainty provided by the GINS kinematic solutions, and ϵ_{ant} is a 1.95 cm uncertainty in manual antenna offset measurement. Average PT WSE ϵ was 8 cm with a range of 4 cm in lakes #2 and #11 to 29 cm in #15. PT WSEs are summarized in Table 2.

We also collected longitudinal profiles of WSE on the Yukon River and a lateral distributary channel (Figure 1a) using a custom engineered GPS system mounted on a SonTek/YSI Hydroboard II (Figure 1d). This custom GPS system consolidates a Trimble R5700 or R7 GPS receiver, a Trimble Zephyr Antenna, and a 12-volt power supply into a ruggedized waterproof housing with external cable and antenna ports. On 15 June 2015, coincident with the AirSWOT overflight, we escorted this GPS drifter down an ~82-km reach of the Yukon River behind a motorized river boat (Figure 1d). The GPS sampling interval results in ~1 GPS profile collection per ~100 m. The same postprocessing and differential corrections were applied. A constant 53.15 ± 2.15 cm vertical offset was subtracted from the processed data to account for the distance from the GPS antenna to the water surface. We refer to corrected and processed GPS surveys in rivers as GPS WSE. These data are provided in Data Set S1.

2.4. Permafrost and Topographic Control on Spatial Variability of WSE

Motivated by the impact of permafrost thaw on surface and groundwater fluxes (Smith et al., 2007; Walvoord et al., 2012) and the associated importance of Arctic and Boreal wetlands in greenhouse gas cycling (Wik et al., 2016), we use AirSWOT to demonstrate the possible impact of permafrost presence on spatial patterns in lake WSE across the YFB (see section 4.2.3). First, we grid our study domain into 5 km × 5 km cells and remove lakes from the land surface DEM. Next, we compare lake WSE variability (WSE_v), defined as the standard deviation of lake WSEs within each 5 km × 5 km cell, with surrounding topographic variability (DEM_v),

defined as the standard deviation of land surface heights (Ascione et al., 2008) within the same 5 km × 5 km grid cell. To quantify the comparative magnitudes of WSE_v and surrounding landscape roughness, we define a dissimilarity ratio (d) as

$$d = \frac{\sqrt{WSE_v}}{\sqrt{DEM_v}} - 1.$$

A $d < 1$ signifies that DEM_v exceeds WSE_v, which we interpret as the hydraulic gradient being influenced primarily by regional topography. A $d > 1$ suggests lake WSE_v exceeds DEM_v, which we interpret as the hydraulic gradient being influenced by factors additional to regional topography, in particular permafrost presence as modeled by (Pastick et al., 2013; Figure 7).

3. Results

3.1. AirSWOT Lake WSE Validation

AirSWOT and PT WSEs in 13 lakes are compared in Figures 2a and 2b. The absolute difference between PT and AirSWOT WSE ranges from 1 to 58 cm, with a mean difference of 25 cm, a standard deviation of 20 cm, and RMSE of 21 cm. Five of 13 lakes had open water areas of at least 1 km^2, and three of these five lakes had AirSWOT WSE within ±10 cm of PT WSE. Three lakes had open water areas between 0.0625 and 1 km^2, and none of these lakes had AirSWOT WSE within ±25 cm PT WSE. Two of the remaining five lakes smaller than 0.0625 km^2 had AirSWOT WSE within ±10 cm PT WSE, which suggests that AirSWOT can map WSE in lakes smaller than SWOT will observe with precisions comparable to SWOT. Differences between AirSWOT and PT WSE for each lake are summarized in Table 2. Note that ground control points were not used for processing these data sets, yet we conservatively estimate that AirSWOT geolocation error is ~1 pixel (see Text S1 and Figure S1).

3.2. AirSWOT River WSE and WSS Validation

AirSWOT and GPS WSE are compared along the Yukon River and a lateral distributary channel for 1-km^2 reaches established at each centerline orthogonal ($n = 16,332$; Figures 2c and 2d). Seventy-two percent of reaches had AirSWOT absolute differences ±10 cm and an RMSE of 8 cm. Similarly, 91% of 0.0625 km^2 ($n = 16,472$) downstream reaches had an AirSWOT absolute difference of ±25 cm and an RMSE of 15 cm (Figure S7). In the context of the SWOT mission accuracy standards, these statistics suggest that AirSWOT can reliably validate SWOT WSE along 1- and 0.0625-km^2 reaches in >70% and >90% of samples, respectively.

SWOT accuracy standards also state that for channels 100 m or wider, WSS should be accurate to ±1.7 cm/km along 10-km reaches. To test AirSWOT precisions against this standard, we removed orthogonal channel cross sections with widths <100 m, established reaches at each centerline orthogonal, and then removed reaches with <80% data coverage ($n = 2,411$, Figure 3a). Sixty-four percent of 10-km reaches had AirSWOT WSS ±1.7 cm/km of GPS WSS (Figure 3f), with an RMSE of 1.5 cm/km and r^2 of 0.8. Note that channel sections had varying braid intensities, tributary inputs, and hydraulic conditions, so some of the reaches in Figure 3 are not ideal for consistent WSS calculations and may contribute to larger uncertainties, particularly in comparison to AirSWOT WSE extractions.

3.3. AirSWOT Precision and Spatial Averaging

AirSWOT precision should improve nonlinearly with increasing spatial averaging area. To test this, we established reaches with variable pixel counts that simulate different sensor resolutions (i.e., for AirSWOT and SWOT) at 0.0625 and 1 km^2 spatial averaging (Table S1). As expected, the RMSE between GPS and AirSWOT decreased nonlinearly with increasing spatial averaging window size (Figure 4a). Similarly, the percent of reaches that met SWOT requirements for 1 km^2 (Figure 4b, red) and 0.0625 km^2 (Figure 4b, blue) area thresholds increased nonlinearly with increasing pixel counts. We do not present a parallel analysis for lakes because many open water lake areas are too small to test the full range of pixel counts.

We also compare the absolute median residual difference between river GPS measurements and nearest neighbor orthogonally averaged AirSWOT WSE by river mask width (Figure 4c). We find that narrow reaches had larger AirSWOT WSE errors. This is consistent with Figures 7a and 7b, suggesting that larger pixel counts
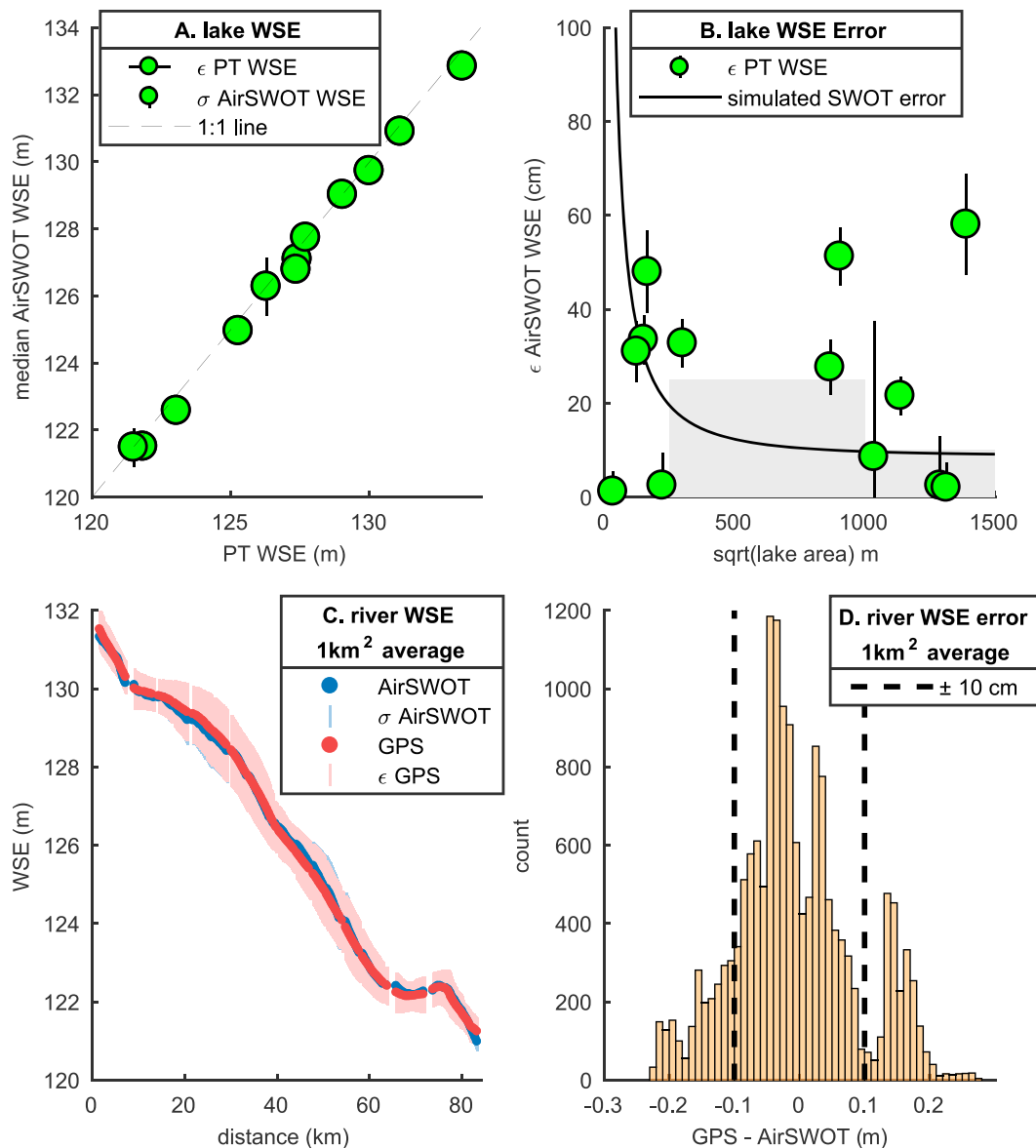
Figure 2. (a, b) Lake water surface elevations (WSEs) calculated from AirSWOT and global positioning system (GPS). (a) AirSWOT WSE is calculated as the median pixel value for each lake, and uncertainty is reported as the standard deviation of pixels. GPS uncertainty is derived from lake pressure transducer and GPS errors; 12 of 13 field lakes are shown; #15 is excluded because it is in the foothills of the White Mountains and has a WSE larger than other lowland lakes. (b) shows the distribution of differences between AirSWOT and GPS for all 13 lakes. Error bars denote uncertainties in field GPS surveys. Gray shading demarcates Surface Water and Ocean Topography (SWOT) mission WSE accuracy requirements. Black line denotes the theoretical SWOT mission error budget (Rodriguez, 2016). (c, d) Yukon River WSE measured by AirSWOT is compared with a coincident GPS WSE survey. (c) plots AirSWOT (blue) for 1-km^2 downstream spatial averages compared with GPS data (red). (D) plots the difference between AirSWOT and GPS for 1-km^2 downstream reaches. The SWOT mission accuracy guidelines states that WSE should be accurate to ±10 cm when spatially averaged over 1-km^2 open water pixels or ±25 cm when spatially averages over 0.0625-km^2 open water pixels. Spatially averaged AirSWOT reaches achieving these precisions fall within dashed lines. See Figure S6 for analogous comparison with 0.0625-km^2 spatial averages.

increased overall AirSWOT precision. Holistically, these results imply that careful consideration of river widths in addition to spatial averaging area is important for future AirSWOT validations of SWOT.

3.4. Hydraulic Gradients

To assess the applicability of AirSWOT for surface water hydrology applications, we mapped hydraulic gradients across all YFB lakes with sufficient AirSWOT data for spatial averaging (see section 3.1) and WSE standard deviations <1 m (Figure 5). There was a dominant east to west hydraulic flow gradient near the Yukon River,
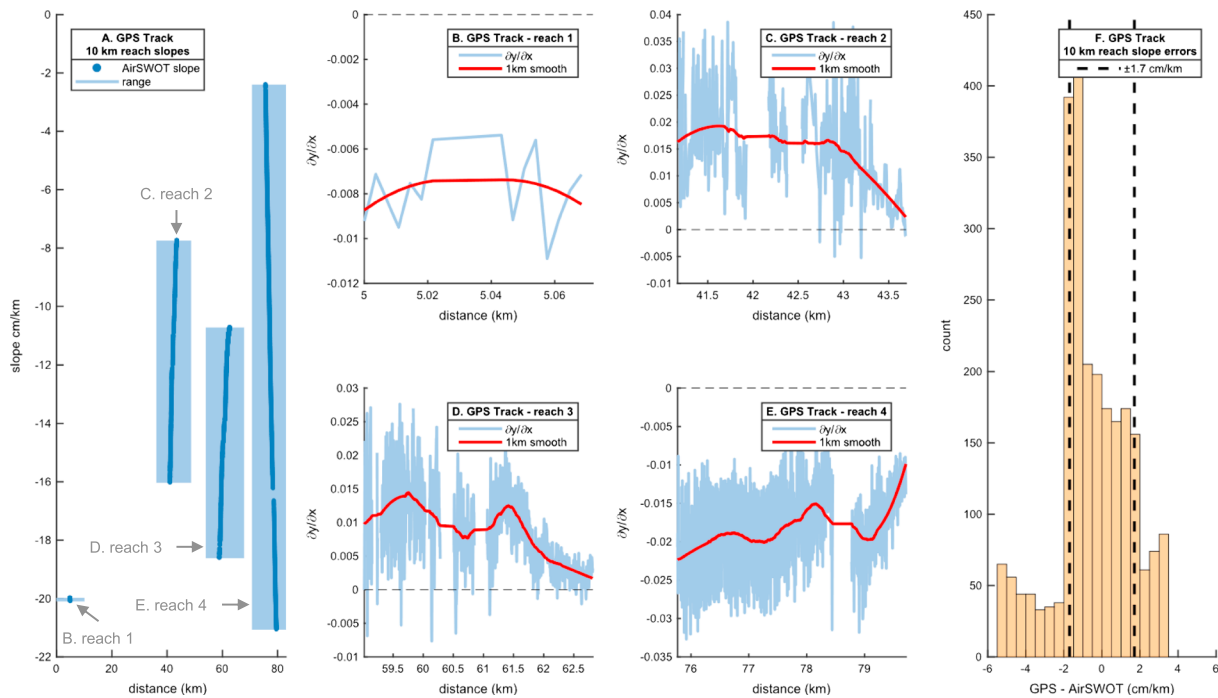
Figure 3. Comparison of Yukon River water surface slope (WSS) calculated using a linear model for downstream water surface elevation profiles from AirSWOT and global positioning system (GPS) data along 10-km reaches. (a) WSS for reaches with channel mask widths of at least 100 m and at least 80% data coverage. (b–e) First derivatives or WSS rate of change by reach. Note that ∂x is constant because WSSs are calculated for 10-km reaches. (f) Difference between AirSWOT and GPS WSS. Dashed lines demarcate 10-km reaches where AirSWOT WSSs are ±1.7-cm/km GPS WSS and thus fall within acceptable SWOT accuracy standards. Removed from this analysis are orthogonal channel cross sections <100 m wide and 10-km reaches with <80% AirSWOT data coverage. In general, Yukon River WSS magnitudes spatially vary, and AirSWOT WSS tends to agree with GPS WSS.

which matches the flow direction of the river and its distributaries. North of the Yukon River the gradient trended from northeast to southwest, while south of the Yukon River it trended southeast to northwest. There was also a north-to-south gradient along the Teedriinjik River and east-to-west gradients along Birch Creek and Beaver Creek (Figure 5). These observed gradients were consistent with the prevailing physiography of the YFB. We present this result as a demonstration that despite poor lake WSE precisions, AirSWOT remains a useful tool for identifying hydrologic gradients in WSE independent of standard topography-based flow routing models.

3.5. Mapping Longitudinal River Profiles and WSS

We used AirSWOT to calculate and compare longitudinal WSE profiles and WSS (Figure 6) along six rivers (the Yukon River GPS WSE track, Yukon River-main channel, Teedriinjik River, Birch Creek-Upper, Birch Creek-Lower, and Beaver Creek) with varying widths, braid intensities, planforms, and orientations relative to the AirSWOT flight paths (Figure 1a). The steepest river is the 24.6-km reach of the Teedriinjik River, which had an average 10-km reach length slope of 0.28 m/km and an overall slope of 0.29 m/km for the full longitudinal profile (Figure 6c). The Teedriinjik River through this reach is highly sinuous and threads into several distributary channels, as it approaches its confluence with the Yukon River. In contrast, Birch Creek-Upper, which was primarily single threaded and had a high degree of connectivity with neighboring lakes, had the most gradual average 10-km reach length slope of 0.11 m/km and an overall slope of 0.11 m/km for the full profile (Figure 6d). Table S2 summarizes the reach length and slope summary statistics for each of these six rivers.

4. Discussion

4.1. AirSWOT Precision, Calibration, and Experiment Design

This is the first empirical investigation of AirSWOT WSE and WSS precisions across a complex lake-river-wetland surface water system. We find that AirSWOT performs better over rivers (RMSE is 8 cm for 1-km^2
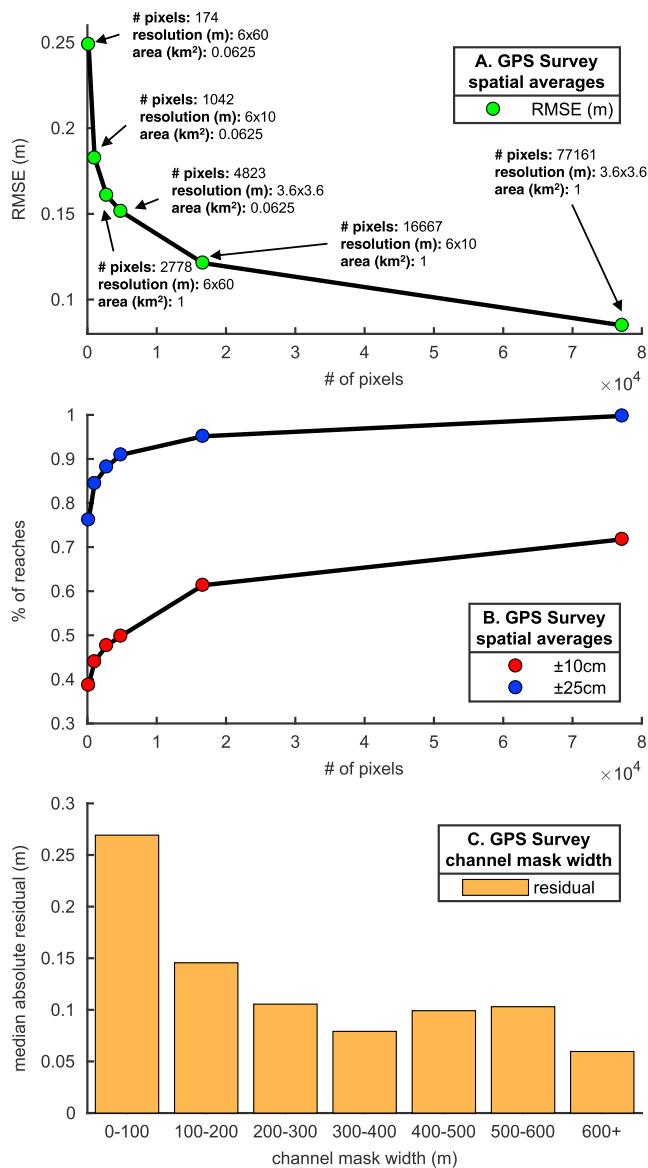
Figure 4. Comparison of (a) root-mean square error (RMSE) of Yukon River AirSWOT water surface elevation (WSE) and (b) Surface Water and Ocean Topography (SWOT) mission accuracy standards by the number of pixels used for downstream spatial averaging. Note that (a) and (b) use the same pixel thresholds (*x*-axis). (c) shows that AirSWOT orthogonal water surface elevation precisions vary with channel mask width.

reaches and 15 cm for 0.0625-km^2 reaches) compared to lakes (RMSE = 21 cm), perhaps due to enhanced surface roughness resulting from a flow-induced turbulence in rivers that is absent in lakes. Furthermore, our results for rivers are similar to those in Altenau et al. (2017) who found RMSE = 9 cm on the Tanana River, Alaska, lending confidence that AirSWOT reproducibly measures river WSE with RMSE <10 cm. Our WSS RMSE = 1.5 cm/km for 10-km reaches at least 100 m wide is similarly commensurate with Altenau et al. (2017), RMSE = 1.0 cm/km. The present study also confirms the Altenau et al. (2017) finding that AirSWOT WSE precisions in rivers vary nonlinearly with channel mask width (Figure 4c). Because the Altenau et al. (2017) study did not investigate lakes, a comparison of the two studies for nonchannelized systems is not possible.

Two additional differences between the present study and Altenau et al. (2017) provide useful insights into AirSWOT precisions. First, Altenau et al. (2017) have a higher data density and significant overlap between AirSWOT flight paths, which permits a data filtering scheme based on magnitude, error, and statistical outliers without direct consideration of incidence angles or SNR. This suggests that the higher data density resulting from the Tanana experiment design helps increase WSE precision, which is consistent with the results we present in Figures 4a and 4b. However, the improvement is incremental, given the similarity in RMSE between the two studies. Second, the YFB AirSWOT flight lines are oriented perpendicularly to the Yukon River, whereas AirSWOT was flown parallel to the study river in Altenau et al. (2017). This results in data gaps in the downstream profiles presented here (e.g., gaps at ~10, ~65, and ~75 km in Figure 2c). This suggests that future AirSWOT campaigns should design airborne flight experiments that maximize spatial overlap between paths while also orienting flight paths parallel to the overall river course direction.

While AirSWOT WSE precisions in rivers generally meet or exceed SWOT standards, the RMSE = 21 cm found here for lake WSE is less encouraging, particularly from a SWOT validation perspective. However, from an airborne remote sensing perspective, these precisions remain high, especially considering no additional ground calibrations were used in AirSWOT data processing. The AirSWOT InSAR processor applies bundle adjustments to correct for aircraft movement that produces along- and cross-track height anomalies. However, additional calibrations such as height correction using ground-based GPS surveys could be applied to further increase the derived WSE precision.

It is also important to emphasize that despite technological similarities to other airborne SARs, AirSWOT remains an experimental sensor and thus research into sensor calibrations and improvements to the AirSWOT InSAR processor are ongoing (Altenau et al., 2017). Furthermore, environmental conditions such as turbulence and wind speed influence water surface roughness (Moller et al., 2000), increasing radar backscatter and SNR thereby improving the derived WSE measurements. We lack localized measurements of wind speed at the water-air interface during the 15 June 2015 AirSWOT surveys to infer instantaneous wind conditions over the lakes studied here. Wind speeds on 15–16 June 2015 at the Fort Yukon Airport, which is ~13 km from the western boundary of our study area, were unremarkable: ranging from 0 to 10.3 m/s with a mean of 2.9 m/s (www.ncdc.noaa. gov). River turbulence provides a water surface roughening mechanism that is absent in lakes. Future field studies should consider assessing water surface roughness, especially wind roughening of lakes, as an added factor determining AirSWOT and SWOT WSE precisions.
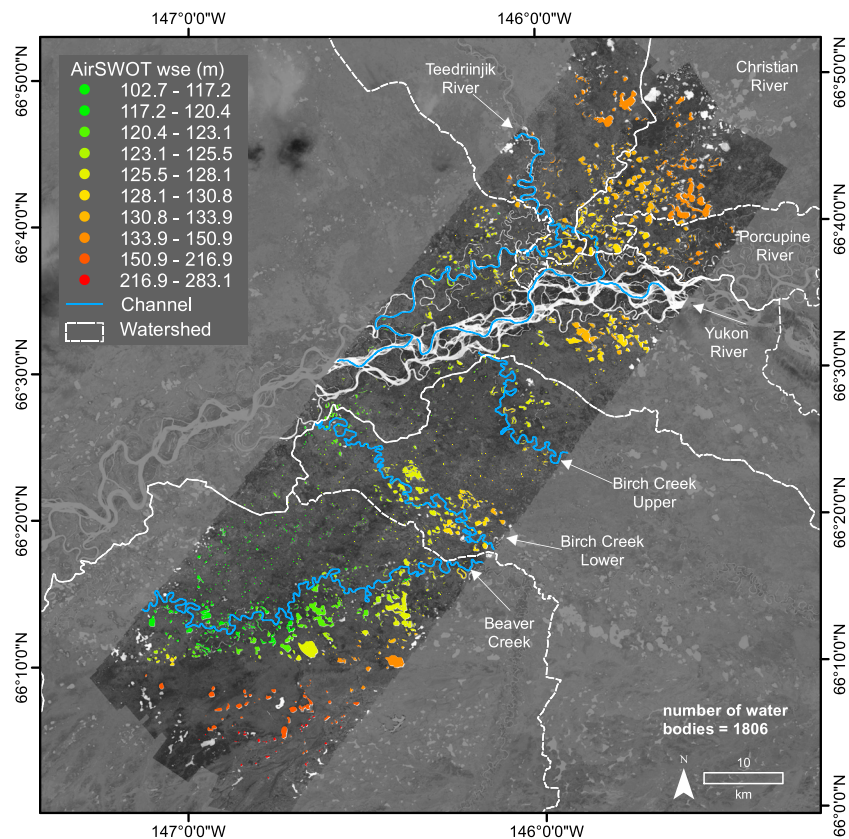
Figure 5. A map of lake AirSWOT water surface elevations (WSEs). Lakes with AirSWOT WSE standard deviations 1 m or more are removed from analysis. White dashed lines show hydrologic divides from the watershed boundary data set (Table 1).

4.2. Scientific Applications of AirSWOT Slope and WSE Measurements Over Rivers and Lakes

AirSWOT, as a novel remote sensing technology independent of SWOT, offers a range of scientific applications that may advance hydraulic, geochemical, and water management aspects of hydrological research. We present four examples here: (1) detection of WSS and rates of change of WSS at reach-relevant scales, (2) comparison of longitudinal profiles for characterizing catchment geomorphic processes and quantifying river discharge, (3) assessment of permafrost influence on WSE in Yukon Flats lakes, and (4) detecting small changes in lake storage that cannot currently be observed from space.

4.2.1. WSS and Rates-of-Change for Investigating River Hydraulics, Reaeration, and Fluvial Geomorphology

River slopes are often calculated by fitting a polynomial between point-based measurements spaced along a reach. This approach is enabled by in situ river gages that monitor WSE continuously, in concert with intermittent satellite altimetry measurements (e.g., Alsdorf et al., 2007; Birkett et al., 2002; Bonnema et al., 2016; Frappart et al., 2006). However, both approaches are limited by sparse measurements, or distant spacing between stream gages and the along track spacing of altimeter footprints. This reduces accuracy of the fitted polynomial and may also miss backwaters, slope breaks, and other real-world hydraulic features present between gaging stations or altimeter tracks. AirSWOT transcends such limitations by mapping WSE at 3.6-m spatial resolution (Figure 6), a spatially dense data set (Figures 3a–3e) from which interesting WSS phenomena are revealed. For example, we find nonmonotonic WSS decays along several reaches of our river GPS surveys, including slopes that are much steeper ~5-km downstream (reach 1, Figure 3a) than they are ~40-km downstream (reach 2, Figure 3a). The spatially dense quality of AirSWOT thus reveals the true WSS between 0- and 10.07-km downstream to range from 19.98 to 20.10 cm/km for 10-km reaches, followed by a slope range of 7.75 to 16.03 cm/km for 10-km reaches established between 36.17- and 48.69-km downstream distance. In contrast, if only two equally spaced point-based WSEs were available at the upper and
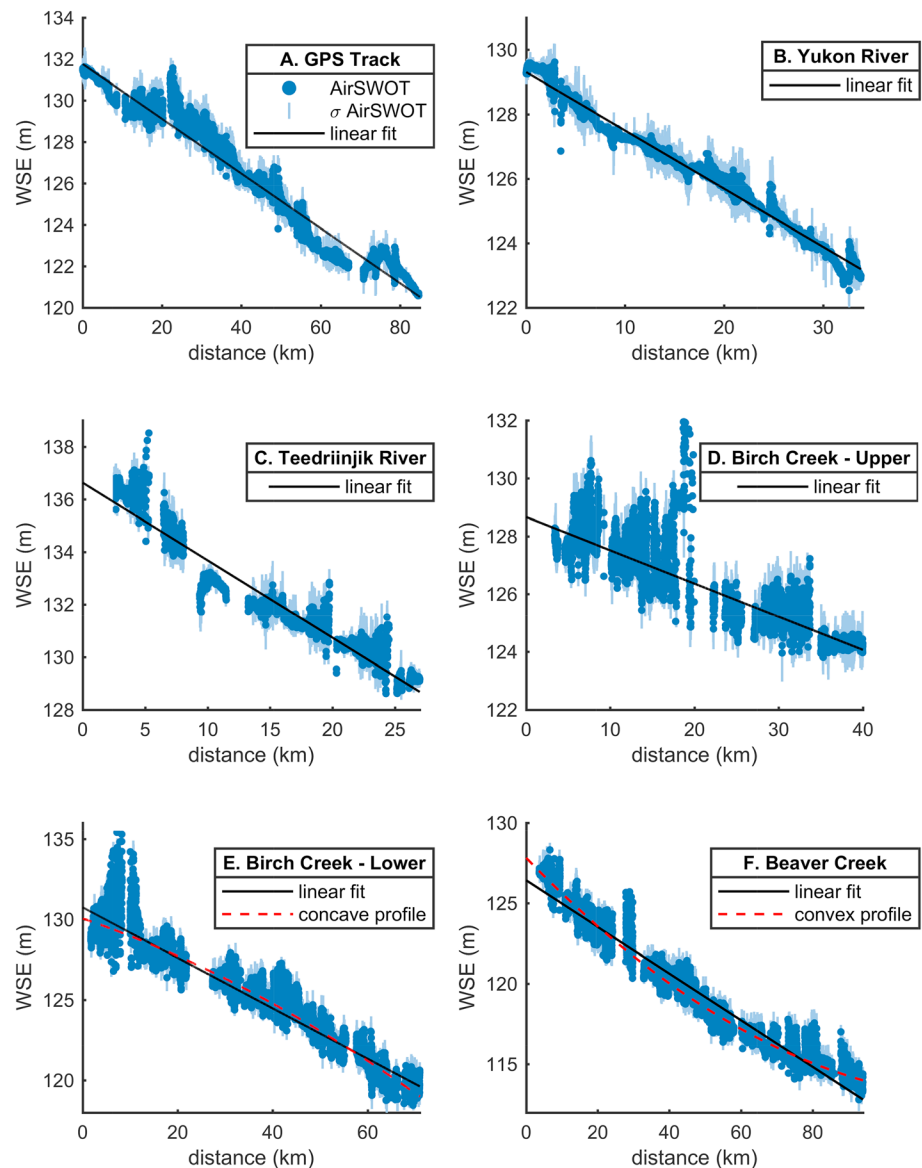
Figure 6. Downstream water surface elevation (WSE) profile for the (a) global positioning system (GPS) survey track, (b) the main stem of the Yukon River, (c) the Teedriinjik River, (d) Birch Creek-Upper, (e) Birch Creek-Lower, and (f) Beaver Creek. AirSWOT values are orthogonal averages after data quality filters (section 3.1) and removal of orthogonals with WSE standard deviations >1 m.

lower ends of these reach (analogous to existing field and altimeter-based techniques), the derived slopes would be 17.21 and 7.94 cm/km, respectively.

Quantifying WSS and spatial rates of change in WSS are also important for water quality modeling and investigating geochemical fluxes in rivers. To that end, Figures 3b–3e plot the first derivatives or the rate of change between 10 km reach length slopes as a function of downstream distance. To clarify spatial patterns in rates-of-change, these first derivatives (Figures 3b–3e, blue) are smoothed (Figure 3b–3e, red) using a Savitzky-Golay or quadratic polynomial filter. These plots emphasize that the rate of change in WSS can be drastic over short downstream distances, for example, flattening by approximately a factor of two over just ~5 km (Figure 3e). One particularly relevant application for mapping phenomena like this is mapping reaeration or in-channel oxygen absorption at the water surface (Bennett & Rathburn, 1972). WSS is used to calculate reaeration coefficients (Melching & Flores, 1999; Parker & Gay, 1987), while understanding the rate of
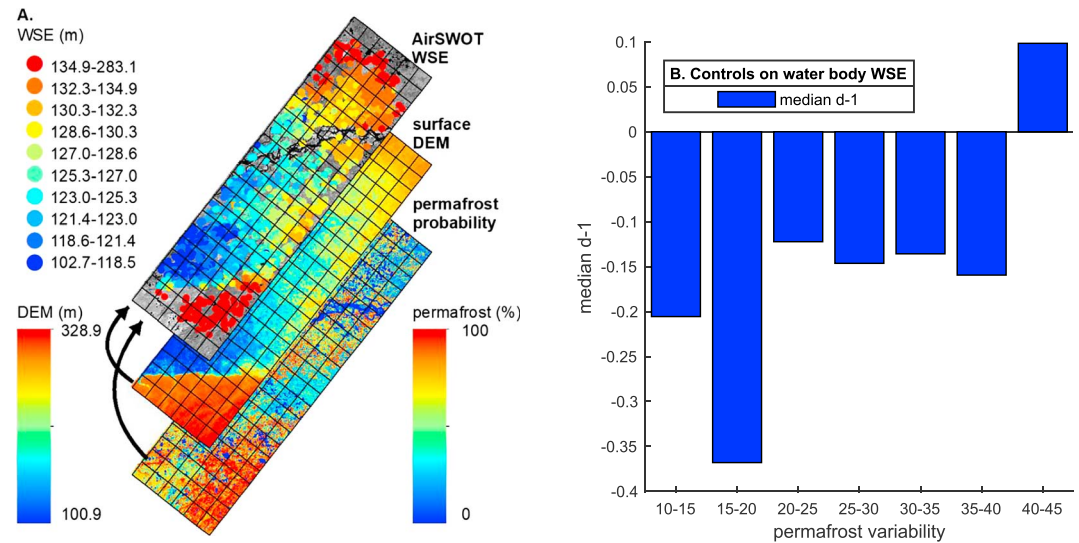
Figure 7. Examination of topographic and permafrost control on lake water surface elevation (WSE) variability. The land surface digital elevation model (DEM) is from Yamazaki et al. (2017) and probability of permafrost presence is from Pastick et al. (2013).

change in WSS enables investigation of reaeration across large spatial scales. More generally, it follows that AirSWOT, and eventually SWOT, may assist in calculating more detailed patterns of WSS and rates of change, which are important not only for reaeration but also for spatial variations in flow velocity, turbidity, discharge, sediment transport, and river planform evolution (e.g., Dade & Friend, 1998; LeFavour & Alsdorf, 2005; Leopold, 1953).

4.2.2. Longitudinal Profiles, Catchment Geomorphology, and Discharge Retrieval

The longitudinal profile of a river is controlled by discharge and sedimentation (Flint, 1974; Knighton, 1998; Leopold et al., 1964; Mackin, 1948) and is important for investigating basin geomorphology (Knighton, 1998) and tectonic deformation (Allen et al., 2013; Kirby & Whipple, 2012). The AirSWOT WSE measurements reported here indicate a concave profile for Birch Creek-Lower (Figure 6e) but a convex profile for Beaver Creek (Figure 6f). River profiles generally tend to be concave (Knighton, 1998; Leopold et al., 1964), thus the notable convexity of Birch Creek is interesting. Mechanisms that control profile convexity include channel roughness, sedimentation, tectonic deformation, and/or geologic events (Knighton, 1998). The neighboring Birch and Beaver creek watersheds both drain the White Mountains to the south and meander across the YFB before joining the Yukon River downstream of our study area. Three plausible explanations for the different profiles we observe include increased sediment mobilization to channels, river avulsions, and/or differing tectonics in catchment headwaters. These explanations are speculative and require further investigation. However, Figure 6 illustrates the types of geomorphic hypotheses that can emerge from novel AirSWOT WSE and WSS mappings of the longitudinal profiles of rivers. Finally, if repeated AirSWOT mappings are conducted, temporal variations in WSS may be inverted to estimate river discharge (Durand et al., 2014, 2016; Garambois & Monnier, 2015; Oubanas et al., 2018).

4.2.3. Topographic and Permafrost Control on WSE Variability in the YFB

Boreal and Arctic lakes are a significant source and emitter of methane (Wik et al., 2016), while future permafrost thaw may boost methane emissions by >3.4 ± 0.08 petagrams of carbon (PgC) from pan-Arctic lakes by the end of this century (Tan & Zhuang, 2015). Furthermore, near-surface permafrost thaw impacts lake volume change more than thaw depth (Jepsen et al., 2013), therefore YFB lakes are particularly vulnerable to warming subsurface temperatures due to the area's shallow aquifer and discontinuous permafrost (Jepsen et al., 2016). We use AirSWOT to demonstrate the possible impact of permafrost presence on spatial patterns in lake WSE across the YFB. We find that where there is low variability in permafrost state (e.g., mostly permafrost or mostly nonpermafrost), d (dissimilarity ratio, see section 2.4) tends to be <1 and thus prevailing topography appears to dominate the hydraulic gradient. However, as variability in permafrost presence increases, topography no longer dominates the hydraulic gradient (Figure 7). If true, this raises the exciting

possibility that areas of permafrost disturbance may be inferred from spatially dense mapping of WSE. However, we emphasize that the permafrost variability bin in Figure 7b with $d > 0$ represents only 15 lakes in one grid cell. As such, this simple analysis is presented as an illustrative demonstration of a potential scientific utility for AirSWOT and SWOT, rather than a definitive study on the impact of permafrost presence on hydraulic gradients across the YFB.

4.2.4. Detecting Changes in Lake Volume Not Currently Observable From Space

Recent advances in passive spaceborne remote sensing technologies such as Planet's CubeSat-based optical constellation and other visible/infrared submeter resolution sensor constellations (e.g., GeoEye-1 and WorldView-1/2/3/4) enable near real time mapping of the world. Despite limitations in data quality and solar/cloud conditions, these sensors are useful in hydrological sciences, particularly for mapping open water extents (Cooley et al., 2017). Nonetheless, they are not capable of directly measuring WSE, volume change, or flux.

The current spaceborne solution for estimating volumetric changes in surface water is laser or radar altimetry in combination with optical measurements of lake area. This approach has been used to track flux in lakes since the early 1990s (Gao et al., 2012). For example, ICESat (Zhang et al., 2011) and the forthcoming ICESat-2 can measure lake WSE. But repeat times are >90 days (https://icesat-2.gsfc.nasa.gov/science/specs), which is insufficient for tracking surface water dynamics, especially in seasonally frozen systems across the Arctic and sub-Arctic. Radar altimetry WSE measurements can achieve ~2-cm accuracies (Crétaux et al., 2009), but lakes with minimal topographic interference/acceptable roughness characteristics are required for such fidelity. Additionally, altimeter measurements are nadir pointing and make profile rather than swath measurements, meaning they must be gridded to be used in mapping applications (Crétaux et al., 2016). Another major limitation is that altimeters can only observe large lakes. For example, Crétaux et al. (2016) list altimetric WSE errors and areas for 24 lakes. Errors range from 3 to 85 cm, but the smallest lake measured was 350 km^2 with an RMSE = 64 cm. Arsen et al. (2015) further demonstrate that altimeters can map WSE in lakes as short as 3.3-km along-track, but with an RMSE range of 12–99 cm.

In contrast, the lakes in our YFB study area vary in size from 55.92 m^2 to 3.26 km^2 and thus would not be observable with radar altimeter-based remote sensing. Also, AirSWOT can map lake WSEs with an overall RMSE of 21 cm, which is within the range of accuracies quantified over much larger lakes using radar altimetry. SWOT will observe lakes that are ≥0.0625 km^2 and potentially as small as 0.01 km^2. Only ~18% (489 of 2,786) of the lakes in our study are ≥0.0625 km^2 and *will* be observable by SWOT while only ~51% (1,417 of 2,786) of lakes are ≥0.01 km^2 and *may* be observable by SWOT. Thus, the complex lake-river-wetland dynamics of the YFB (and similar Arctic and Boreal wetlands) occur at scales that are currently only observable by AirSWOT-like active airborne remote sensing technologies.

5. Conclusion

We conclude that AirSWOT offers utility as a validation tool for SWOT measurements of WSE and WSS in rivers and as an independent experimental technology for scientific surface water hydrology studies. AirSWOT river WSEs meet or exceed SWOT mission standards, and while lake WSEs remain unsatisfactory, improvements to the InSAR processor, enhanced data calibrations, and modifications to experiment design are likely to improve data quality in the future. Independent of SWOT, we demonstrate that AirSWOT enables investigation of complex lake/wetland hydraulic gradients, remote estimation of river discharge, water quality/geochemical flux, channel sedimentation and geomorphic processes, influence of permafrost on surface water storage, and for mapping volumetric surface water changes and fluxes not detectable by current or planned satellite remote sensing technologies.

References

Allen, G. H., Barnes, J. B., Pavelsky, T. M., & Kirby, E. (2013). Lithologic and tectonic controls on bedrock channel form at the northwest Himalayan front. *Journal of Geophysical Research: Earth Surface*, 118, 1806–1825. https://doi.org/10.1002/jgrf.20113

Alsdorf, D. E., Rodríguez, E., & Lettenmaier, D. P. (2007). Measuring surface water from space. *Reviews of Geophysics*, 45, RG2002. https://doi.org/10.1029/2006RG000197

Altenau, E. H., Pavelsky, T. M., Moller, D., Lion, C., Pitcher, L. H., Allen, G. H., Bates, P. D., et al. (2017). AirSWOT measurements of river water surface elevation and slope: Tanana River, AK. *Geophysical Research Letters*, 44, 181–189. https://doi.org/10.1002/2016GL071577

Arsen, A., Crétaux, J. -f., & del Rio, R. A. (2015). Use of SARAL/AltiKa over Mountainous Lakes, Intercomparison with Envisat Mission. *Marine Geodesy*, 38, 534–548. https://doi.org/10.1080/01490419.2014.1002590

Ascione, A., Cinque, A., Miccadei, E., Villani, F., & Berti, C. (2008). The Plio-Quaternary uplift of the Apennine chain: New data from the analysis of topography and river valleys in Central Italy. *Geomorphology*, *102*(1), 105–118. https://doi.org/10.1016/j.geomorph.2007.07.022

Bennett, J. P., & Rathbun, R. E. (1972). Reaeration in open-channel flow. *Geological Survey Professional Paper*, *737*, 86.

Biancamaria, S., Lettenmaier, D. P., & Pavelsky, T. M. (2016). The SWOT mission and its capabilities for land hydrology. *Surveys in Geophysics*, *37*(2), 307–337. https://doi.org/10.1007/s10712-015-9346-y

Birkett, C. M., Mertes, L. A., Dunne, T., Costa, M. H., & Jasinski, M. J. (2002). Surface water dynamics in the Amazon Basin: Application of satellite radar altimetry. *Journal of Geophysical Research*, *107*(D20), 8059. https://doi.org/10.1029/2001JD000609

Bonnema, M. G., Sikder, S., Hossain, F., Durand, M., Gleason, C. J., & Bjerklie, D. M. (2016). Benchmarking wide swath altimetry-based river discharge estimation algorithms for the Ganges river system. *Water Resources Research*, *52*, 2439–2461. https://doi.org/10.1002/2015WR017296

Brabets, T. P., Wang, B., & Meade, R. H. (2000). Environmental and hydrologic overview of the Yukon River Basin, Alaska and Canada. Water-Resources Investigations Report *99–4204*.

Cisneros, B. E. J., Oki, T., Arnell, N. W., Benito, G., Cogley, J. G., Döll, P., et al. (2014). Freshwater resources. *Climate Change 2014: Impacts, Adaptation, and Vulnerability. Part A: Global and Sectoral Aspects. Contribution of Working Group II to the Fifth Assessment Report of the Intergovernmental Panel on Climate Change*. Cambridge, United Kingdom: Cambridge University Press. Retrieved from http://ipcc-wg2.gov/AR5/report/full-report/

Cooley, S. W., Smith, L. C., Stepan, L., & Mascaro, J. (2017). Tracking dynamic northern surface water changes with high-frequency planet CubeSat imagery. *Remote Sensing*, *9*(12), 1–21. https://doi.org/10.3390/rs9121306

Crétaux, J. F., Abarca-del-Río, R., Bergé-Nguyen, M., Arsen, A., Drolon, V., Clos, G., & Maisongrande, P. (2016). Lake volume monitoring from space. *Surveys in Geophysics*, *37*(2), 269–305. https://doi.org/10.1007/s10712-016-9362-6

Crétaux, J. F., Calmant, S., Romanovski, V., Shabunin, A., Lyard, F., Bergé-Nguyen, M., Cazenave, A., et al. (2009). An absolute calibration site for radar altimeters in the continental domain: Lake Issykkul in Central Asia. *Journal of Geodesy*, *83*(8), 723–735. https://doi.org/10.1007/s00190-008-0289-7

Dade, W. B., & Friend, P. F. (1998). Grain-size, sediment-transport regime, and channel slope in alluvial Rivers. *The Journal of Geology*, *106*(6), 661–676. https://doi.org/10.1086/516052

Durand, M., Gleason, C. J., Garambois, P. A., Bjerklie, D., Smith, L. C., Roux, H., Rodriguez, E., et al. (2016). An intercomparison of remote sensing river discharge estimation algorithms from measurements of river height, width, and slope. *Water Resources Research*, *52*, 4527–4549. https://doi.org/10.1002/2015WR018434

Durand, M., Neal, J., Rodríguez, E., Andreadis, K. M., Smith, L. C., & Yoon, Y. (2014). Estimating reach-averaged discharge for the River Severn from measurements of river water surface elevation and slope. *Journal of Hydrology*, *511*, 92–104. https://doi.org/10.1016/j.jhydrol.2013.12.050

Estey, L. H., & Meertens, C. M. (1999). TEQC: The multi-purpose toolkit for GPS/GLONASS data. *GPS Solutions*, *3*(1), 42–49. https://doi.org/10.1007/PL00012778

Fisher, G. B., Amos, C. B., Bookhagen, B., Burbank, D. W., & Godard, V. (2012). Channel widths, landslides, faults, and beyond: The new world order of high- spatial resolution Google Earth imagery in the study of earth surface processes. In S. J. Whitmeyer, J. E. Bailey, D. G. De Paor, & T. Ornduff (Eds.), *Google Earth and Virtual Visualizations in Geoscience Education and Research*. *Geological Society of America Special Paper*, *492*, 1–22. https://doi.org/10.1130/2012.2492(01)

Fisher, G. B., Bookhagen, B., & Amos, C. B. (2013). Channel planform geometry and slopes from freely available high-spatial resolution imagery and DEM fusion: Implications for channel width scalings, erosion proxies, and fluvial signatures in tectonically active landscapes. *Geomorphology*, *194*, 46–56. https://doi.org/10.1016/j.geomorph.2013.04.011

Fjørtoft, R., Gaudin, J. M., Pourthié, N., Lalaurie, J. C., Mallet, A., Nouvel, J. F., et al. (2014). KaRIn on SWOT: Characteristics of near-nadir Ka-band interferometric SAR imagery. *IEEE Transactions on Geoscience and Remote Sensing*, *52*(4), 2172–2185. https://doi.org/10.1109/TGRS.2013.2258402

Flint, J. J. (1974). Stream gradient as a function of order, magnitude, and discharge. *Water Resources Research*, *10*(5), 969–973. https://doi.org/10.1029/WR010i005p00969.

Frappart, F., Calmant, S., Cauhopé, M., Seyler, F., & Cazenave, A. (2006). Preliminary results of ENVISAT RA-2-derived water levels validation over the Amazon basin. *Remote Sensing of Environment*, *100*(2), 252–264. https://doi.org/10.1016/j.rse.2005.10.027

Gao, H., Birkett, C., & Lettenmaier, D. P. (2012). Global monitoring of large reservoir storage from satellite remote sensing. *Water Resources Research*, *48*, W09504. https://doi.org/10.1029/2012WR012063

Garambois, P.-A., & Monnier, J. (2015). Advances in water resources inference of effective river properties from remotely sensed observations of water surface. *Advances in Water Resources*, *79*, 103–120. https://doi.org/10.1016/j.advwatres.2015.02.007

Gleason, C. J., Garambois, P.-A., & Durand, M. T. (2017). Tracking river flows from space. *Eos*, *98*. https://doi.org/10.1029/2017EO078085

Glennie, C. (2018). Arctic high-resolution elevation models: Accuracy in sloped and vegetated terrain. *Journal of Surveying Engineering*, *144*(1), 1–9. https://doi.org/10.1061/(ASCE)SU.1943-5428.0000245

Gulbrandsen, M. L., Minsley, B. J., Ball, L. B., & Hansen, T. M. (2016). Semiautomatic mapping of permafrost in the Yukon Flats, Alaska. *Geophysical Research Letters*, *43*, 12,131–12,137. https://doi.org/10.1002/2016GL071334

Hopkinson, C., Crasto, N., Marsh, P., Forbes, D., & Lesack, L. (2011). Investigating the spatial distribution of water levels in the Mackenzie Delta using airborne LiDAR. *Hydrological Processes*, *25*(19), 2995–3011. https://doi.org/10.1002/hyp.8167

Jenson, J. R. (2000). *Remote sensing of the environment: an Earth resource perspective*. Upper Saddle River, NJ: Prentice Hall Inc.

Jepsen, S. M., Voss, C. I., Walvoord, M. A., Minsley, B. J., & Rover, J. (2013). Linkages between lake shrinkage/expansion and sublacustrine permafrost distribution determined from remote sensing of interior Alaska, USA. *Geophysical Research Letters*, *40*, 882–887. https://doi.org/10.1002/grl.50187

Jepsen, S. M., Walvoord, M. A., Voss, C. I., & Rover, J. (2016). Effect of permafrost thaw on the dynamics of lakes recharged by ice-jam floods: Case study of Yukon Flats, Alaska. *Hydrological Processes*, *30*(11), 1782–1795. https://doi.org/10.1002/hyp.10756

Kirby, E., & Whipple, K. X. (2012). Expression of active tectonics in erosional landscapes. *Journal of Structural Geology*, *44*, 54–75. https://doi.org/10.1016/j.jsg.2012.07.009

Knighton, D. (1998). *Fluvial forms and processes: A new perspective*. London and New York: Hoder Education.

LeFavour, G., & Alsdorf, D. (2005). Water slope and discharge in the Amazon River estimated using the shuttle radar topography mission digital elevation model. *Geophysical Research Letters*, *32*, L16308. https://doi.org/10.1029/2005GL023491

Leopold, L. B. (1953). Downstream change of velocity in rivers. *American Journal of Science*, *251*(8), 606–624. https://doi.org/10.2475/ajs.251.8.606.

Leopold, L. B., Wolman, G. M., & Miller, J. P. (1964). *Fluvial processes in geomorphology*. New York, NY: Dover Publications, Inc.

Li, J., & Sheng, Y. (2012). An automated scheme for glacial lake dynamics mapping using Landsat imagery and digital elevation models: A case study in the Himalayas. *International Journal of Remote Sensing*, *33*(16), 5194–5213. https://doi.org/10.1080/01431161.2012.657370

Mackin, J. H. (1948). Concept of the Graded River. *Bulletin of the Gelogical Society of America*, *59*(5), 463–512. https://doi.org/10.1130/0016-7606(1948)59[463:COTGR]2.0.CO;2

Marty, J. C., Loyer, S., Perosanz, F., Mercier, F., Bracher, G., Legresy, B., et al. (2011). GINS: The CNES/GRGS GNSS scientific software. In *3rd International Colloquium Scientific and Fundamental Aspects of the Galileo Programme, ESA Proceedings WPP326*, 31 August - 2 September 2011, Copenhagen, Denmark.

Mcfeeters, S. K. (1996). The use of the normalized difference water index (NDWI) in the delineation of open water features. *International Journal of Remote Sensing*, *17*(7), 1425–1432. https://doi.org/10.1080/01431169608948714

Melching, C. S., & Flores, H. E. (1999). Reaeration equations derived from U.S. Geological Survey database. *Journal of Environmental Engineering*, *125*(5), 407–414. https://doi.org/10.1061/(ASCE)0733-9372(1999)125:5(407)

Minsley, B. J., Abraham, J. D., Smith, B. D., Cannia, J. C., Voss, C. I., Jorgenson, M. T., Walvoord, M. A., et al. (2012). Airborne electromagnetic imaging of discontinuous permafrost. *Geophysical Research Letters*, *39*, L02503. https://doi.org/10.1029/2011GL050079

Moller, D. K., Mourad, P. D., & Frasier, S. J. (2000). Field observations of radar backscatter from the ocean surface under low wind speed conditions. *Journal of Geophysical Research*, *105*(C10), 24,059–24,069. https://doi.org/10.1029/2000JC900103

Neeck, S. P., Lindstrom, E. J., Vaze, P. V., & Fu, L.-L. (2012). Surface water and ocean topography (SWOT) mission. In *Sensors, Systems and Next-Generation Satellites XVI, Proceedings of SPIE 8533* (pp. 85330G-1–85330G-10). Edinburgh, UK. https://doi.org/10.1117/12.981151

Oubanas, H., Gejadze, I., Malaterre, P. O., & Mercier, F. (2018). River discharge estimation from synthetic SWOT-type observations using variational data assimilation and the full saint-Venant hydraulic model. *Journal of Hydrology*, *559*, 638–647. https://doi.org/10.1016/j.jhydrol.2018.02.004

Parker, G. W., & Gay, F. B. (1987). A procedure for estimating reaeration coefficients for Massachusetts streams. U.S. *Geological Survey Water Resources Investigations Report*, 86–4111. U.S. Geological Survey.

Pastick, N. J., Jorgenson, M. T., Wylie, B. K., Minsley, B. J., Ji, L., Walvoord, M. A., Smith, B. D., et al. (2013). Extending airborne electromagnetic surveys for regional active layer and permafrost mapping with remote sensing and ancillary data, Yukon Flats Ecoregion, Central Alaska. *Permafrost and Periglacial Processes*, *24*(3), 184–199. https://doi.org/10.1002/ppp.1775

Pavelsky, T. M., & Smith, L. C. (2008). RivWidth: A software tool for the calculation of river width from raster-based imagery. *IEEE Geoscience and Remote Sensing Letters*, *5*(1), 70–73. https://doi.org/10.1109/LGRS.2007.908305

Pekel, J.-F., Cottam, A., Gorelick, N., & Belward, A. S. (2016). High-resolution mapping of global surface water and its long-term changes. *Nature*, *540*(7633), 418–422. https://doi.org/10.1038/nature20584

Pitcher, L. H., Smith, L. C., Pavelsky, T. M., Fayne, J. V., Cooley, S. W., Altenau, E. H., Moller, D. K., & Arvesen, J. (2018). NASA AirSWOT InSAR, Water Surface Elevations, and CIR water mask, Yukon Flats, Alaska. *ORNL DAAC, Oak Ridge, Tennessee, USA*. https://doi.org/10.3334/ORNLDAAC/1655

Raymond, P. A., Hartmann, J., Lauerwald, R., Sobek, S., McDonald, C., Hoover, M., et al. (2013). Global carbon dioxide emissions from inland waters. *Nature*, *503*(7476), 355–359. https://doi.org/10.1038/nature12760

Rodriguez, E. (2016). Surface water and ocean topography mission (SWOT) project: Science requirements documents. *SWOT NASA/JPL Project*.

Rosen, P. A., Hensley, S., Joughin, I. R., Li, F., Madsen, S. N., Ernesto, R., & Goldstein, R. M. (2000). Synthetic aperture radar interferometry. *Proceedings of the IEEE*, *88*(3), 333–382. https://doi.org/10.1109/5.838084

Sheng, Y., Song, C., Lettenmaier, D. P., & Ke, L. (2016). Where and in what quantity are lakes observable by SWOT? In *American Geophysical Union. Fall Meeting*. San Francisco.

Smith, L. C., Sheng, Y., & MacDonald, G. M. (2007). A first pan-Arctic assessment of the influence of glaciation, permafrost, topography and peatlands on Northern Hemisphere lake distribution. *Permafrost and Periglacial Processes*, *18*(2), 201–208. https://doi.org/10.1002/ppp.

Tan, Z., & Zhuang, Q. (2015). Methane emissions from pan-Arctic lakes during the 21st century: An analysis with process-based models of lake evolution and biogeochemistry. *Journal of Geophysical Research: Biogeosciences*, *120*, 1–13. https://doi.org/10.1002/2015JG003184

Walvoord, M. A., Voss, C. I., & Wellman, T. P. (2012). Influence of permafrost distribution on groundwater flow in the context of climate-driven permafrost thaw: Example from Yukon Flats Basin, Alaska, United States. *Water Resources Research*, *48*, W07524. https://doi.org/10.1029/2011WR011595

Wik, M., Varner, R. K., Anthony, K. W., MacIntyre, S., & Bastviken, D. (2016). Climate-sensitive northern lakes and ponds are critical components of methane release. *Nature Geoscience*, *9*(2), 99–105. https://doi.org/10.1038/ngeo2578

Yamazaki, D., Ikeshima, D., Tawatari, R., Yamaguchi, T., O'Loughlin, F., Neal, J. C., Sampson, C. C., et al. (2017). A high-accuracy map of global terrain elevations. *Geophysical Research Letters*, *44*, 5844–5853. https://doi.org/10.1002/2017GL072874

Zhang, G., Xie, H., Kang, S., Yi, D., & Ackley, S. F. (2011). Monitoring lake level changes on the Tibetan Plateau using ICESat altimetry data (2003-2009). *Remote Sensing of Environment*, *115*(7), 1733–1742. https://doi.org/10.1016/j.rse.2011.03.005